JACS
JOURNAL OF THE AMERICAN CHEMICAL SOCIETY
Article
pubs.acs.org/JACS

Influence of Surface Structure on Single or Mixed Component Self-Assembled Monolayers via in Situ Spectroelectrochemical Fluorescence Imaging of the Complete Stereographic Triangle on a Single Crystal Au Bead Electrode

Zhinan Landis Yu,[†,‡] Jannu Casanova-Moreno,[†,‡] Ivan Guryanov,[§,∥] Flavio Maran,[§] and Dan Bizzotto*[,†,‡]

[†]AMPEL, [‡]Department of Chemistry, University of British Columbia, Vancouver, British Columbia V6T 1Z1, Canada
[§]Department of Chemistry, University of Padova, 35122 Padova, Italy

Supporting Information

ABSTRACT: The use of a single crystal gold bead electrode is demonstrated for characterization of self-assembled monolayers (SAM)s formed on the bead surface expressing a complete set of face centered cubic (fcc) surface structures represented by a stereographic projection. Simultaneous analysis of many crystallographic orientations was accomplished through the use of an in situ fluorescence microscopic imaging technique coupled with electrochemical measurements. SAMs were prepared from different classes of molecules, which were modified with a fluorescent tag enabling characterization of the influence of electrical potential and a direct comparison of the influence of surface structure on SAMs adsorbed onto low index, vicinal and chiral surfaces. The assembly of alkylthiol, Aib peptide and DNA SAMs are studied as a function of the electrical potential of the interface revealing how the organization of these SAMs depend on the surface crystallographic orientation, all in one measurement. This approach allows for a simultaneous determination of SAMs assembled onto an electrode surface onto which the whole fcc stereographic triangle can be mapped, revealing the influence of intermolecular interactions as well as the atomic arrangement of the substrate. Moreover, this method enables study of the influence of the Au surface atom arrangement on SAMs that were created and analyzed, both under identical conditions, something that can be challenging for the typical studies of this kind using individual gold single crystal electrodes. Also demonstrated is the analysis of a SAM containing two components prepared using thiol exchange. The two component SAM shows remarkable differences in the surface coverage, which strongly depends on the surface crystallography enabling estimates of the thiol exchange energetics. In addition, these electrode surfaces enable studies of molecular adsorption onto the symmetry related chiral surfaces since more than one stereographic triangle can be imaged at the same time. The ability to observe a SAM modified surface that contains many complete fcc stereographic triangles will facilitate the study of the single and multicomponent SAMs, identifying interesting surfaces for further analysis.

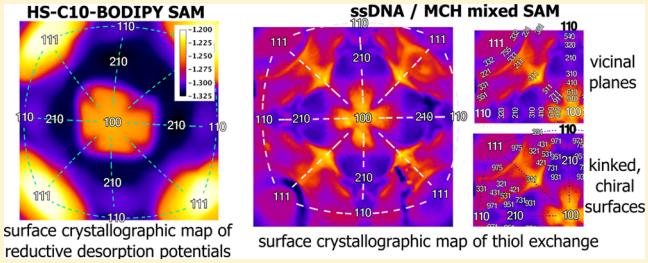

INTRODUCTION

Surface modification of gold by molecular adsorbates is strongly dependent on its atomic surface structure, in particular the atomic arrangement of the gold surface atoms. Studies that investigate the surface crystallography and its influence over the monolayer adsorption are numerous, requiring the creation of many single crystal gold electrodes that are cut and polished and carefully prepared, revealing the surface of interest. This method was pioneered for use in electrochemical studies of gold in the early eighties by Clavilier, Hamelin and Lipkowski[1−7] and is a methodology currently used in electrochemical as well as surface science studies. The preparation and cleaning of these electrode surfaces can be a difficult process, and reproducibility can be challenging, though these issues are currently not problematic as defined procedures exist to create clean and well-defined surfaces for electrochemical studies.[1,3,4,8] The study of molecular adsorption onto various single crystal surfaces of gold has been reported for physisorbed as well as chemisorbed species, in particular for thiol-based self-assembled monolayers (SAMs).[5,9−12] These fundamental studies, mainly on the low index planes (111, 110, 100) as well as the more open 210 surface have shown that adsorbed molecules will form different surface arrangements on these single crystal electrode surfaces.[9,13,14] Importantly, these studies are useful in informing the surface adsorption behavior which influences the morphology of electrodeposited metals in the presence of additives in addition to the growth of particular nanoparticles whose shape requires the presence of additives. One example of the study of the adsorption of a model quarternary ammonium bromide surfactant onto the low index planes of gold[15−17] showed that Br^- has a significant role in

Received: October 10, 2014
Published: December 12, 2014

DOI: 10.1021/ja5104475
J. Am. Chem. Soc. 2015, 137, 276−288

directing the growth of the 111 ends of the nanorods while allowing the 110 or 100 sides to be stabilized.

As demonstrated in the typically irrreproducible nanorod fabrication, the conditions under which the surface modification is performed can have dramatic effects on the monolayer quality or on the nature of the adsorbed monolayer. Small changes or contaminants in the self-assembly solution, small differences in the temperature, or the quality of the surface can create difficulties with the data interpretation. It is quite important to achieve the same assembly condition for each surface to be studied. Invariably, some conditions cannot be exactly controlled, resulting in a distribution in the quality of the SAM.[12] One approach that addresses this problem is to assemble or modify the surface of the electrodes at the same time in the same deposition solution. This is in principle easily achieved if sufficient amount of adsorbate and a multitude of substrates can be gathered, but the characterization performed can also suffer from small differences in the methods used or in the electrochemical conditions employed (whether intentionally controlled or not). The ideal solution to this problem is to prepare and analyze the surfaces under identical conditions. This can be achieved through the use of a single crystal bead surface where a large variety of atomic surface arrangements can be realized.

Gold bead electrodes have been used in previous work to investigate the nature of the reductive desorption process as a function of the surface structure, supported by the work on polished single crystal surfaces and mapping of the surface crystallography.[18] Single crystal bead electrodes prepared from melting and slow cooling has been detailed in literature[1,2,19,20] and are typically used to create surfaces that have large 111 facets, which are then oriented using a laser, and polished resulting in a single crystal 111 surface.[1,21] In principle, a surface of any crystallographic orientation can be created for electrochemical studies with proper orientation and polishing.

The surface of the bead electrodes is composed of a number of surface structures that result from the slow cooling and annealing of the bead surface. In addition to the large 111 facets, the 100 facet should be observed at positions related by fcc symmetry, which can be represented using a stereographic triangle. Here we demonstrate that these Au bead electrodes have surfaces that can be considered as a representation of the surfaces that compose the fcc stereographic triangle. In principle, the bead surface will have almost every idealized surface atom arrangement represented, though surface reconstructions are known to play an important role for some surfaces.[1,4] Realization of this is demonstrated using a fluorophore labeled alkylthiol SAM formed on the surface of a single crystal Au bead electrode. The identification of the various surfaces is achieved through the contrast observed across the bead surface during reductive desorption relying on the known dependence of the desorption potential on surface crystallography. Investigating the role of the characteristics of the adsorbate in the stability of the SAM as a function of the surface crystallography is demonstrated next through the use of an α-aminoisobutyric acid (Aib) peptide SAM which shows significant differences as compared to the alkylthiol SAM as a function of the surface crystallography. Finally, the modification of a SAM through thiol exchange is demonstrated. The competitive displacement or exchange of a thiolated DNA molecule with a SAM composed of a small alkylthiol (mercaptohexanol) clearly shows the strong influence of the underlying surface crystallography on the resulting mixed composition SAM. These studies are only possible using a combination of fluorophore labeled adsorbate and in situ fluorescence microscopic analysis of the electrochemical interface.

EXPERIMENTAL SECTION

Preparation of the Bead Electrodes. The single crystalline gold bead electrode was fabricated from a gold wire (purity >99.999%, 1 mm diameter, Alfa Aesar). The gold wire was heated and melted with a butane torch. The bottom part of the gold wire was kept molten until a gold bead formed and grew to approximately 2−3 mm in diameter. The bead was slowly cooled down and solidified by gently moving the flame away. Then the gold bead was immersed in an aqua regia solution for 15 min to dissolve the superficial layer of Au atoms along with possible impurities. After the cleaning process, the melting and solidifying process was repeated. The flame intensity and position should be well controlled not only to keep the bead molten for about 1 min before cooling down, but also to prevent further growth of the bead. Two more aqua regia cleaning cycles followed by melting and solidifying were performed. A clean single crystalline gold bead can be obtained using the procedures above. Usually, four equally spaced facets can be seen above the equator of the bead (AFM characterization of a 111 facet is presented in Figure S1), which suggests a crystalline gold bead. If this pattern cannot be discerned, the melting and solidifying process can be repeated until the four facet pattern appears. This method has been used extensively to make polished single crystalline Pt electrodes for use in the hanging meniscus arrangement.[1,21]

Cleaning of the Single Crystalline Gold Bead Electrode. Before each SAM preparation, the single crystalline gold bead electrode was heated with butane torch until the bead turned orange (not melted) for approximately 10 s, followed by rinsing in Millipore deionized water (>18 MΩ cm). This heating and rinsing procedure was typically performed 3 times before assembly. After electrochemical measurements in which the SAM was desorbed, the substrate electrode was cleaned with cyclic voltammetry scans, −1.20 V to +0.85 V/AgAgCl, at 200 mV/s for 20 min in a newly prepared $KClO_4$ (doubly recrystallized) electrolyte (pH ≈ 12 (±0.05) adjusted with KOH (Sigma semiconductor grade)). Further cleaning of the electrode surface by gentle electropolishing[22] was required after every five SAM depositions to remove accumulated organic residues that were not removed via flame treatment. Electropolishing was accomplished by polarizing the gold bead at +2.45 V vs Au wire in a 1 M $HClO_4$ solution for 30 s followed by immersion in 1 M HCl solution for 10 s. This was followed by cyclic voltammetry scans, −1.0 V to +1.1 V/AgAgCl at 20 mV/s in a newly prepared $KClO_4$ electrolyte for 10 min.

Materials. The thiol containing adsorbates used were a BODIPY labeled alkylthiol (HS-C10-BODIPY), its synthesis outlined in the literature,[23] a BODIPY labeled Aib peptide (HS-Aib4-BODIPY), its synthesis described in the Supporting Information, and a ssDNA (5′-CTG-TAT-TGA-GTT-GTA-TCG-TGT-GGT-GTA-TTT-3′, from Eurogentec) modified with a thiol attached to a six carbon alkyl linker on the 5′ end and with the AlexaFluor488 dye on the 3′ end. The chemical structures of these thiolated compounds are shown in the Supporting Information (Figure S1).

Deposition of the HS-C10-BODIPY SAM. A clean substrate electrode was immersed in 1 mL of 1 mM HS-C10-BODIPY 1:1 MeOH−$CHCl_3$ solution in a glass vial for 15 min. The modified electrode was then rinsed with the solvent and then water before characterization.

Deposition of the HS-Aib4-BODIPY SAM. A clean substrate electrode was immersed in 50 μL of 1.0 μM HS-Aib4-BODIPY ethanolic solution in a sealed microcentrifuge tube (siliconized, from BioPlas) for 2.0 h. The modified electrode was then rinsed with the solvent and then water before characterization.

Deposition of the MCH-DNA SAM. A clean substrate electrode was immersed in 30 μL of 1.0 mM mercaptohexanol (MCH, Aldrich 99%) in a buffer solution (10 mM Tris, JT Baker, ultrapure) and 100 mM

DOI: 10.1021/ja5104475
J. Am. Chem. Soc. 2015, 137, 276−288

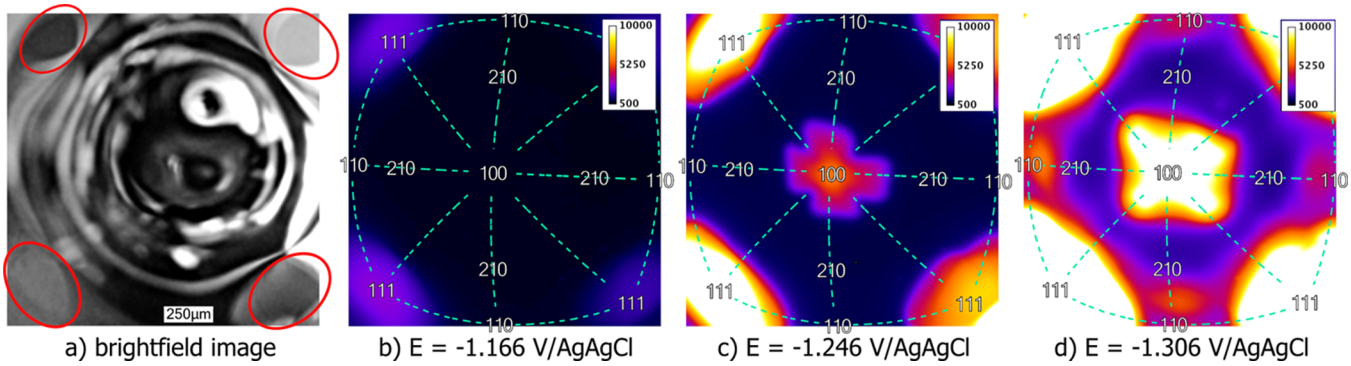

Figure 1. In situ images of the Au bead electrode surface. (a) Brightfield optical image (at open circuit potential) with 111 facets outlined and three fluorescence images of a gold bead electrode at different potentials approximately corresponding to the desorption of the (b) 111, (c) 100 and (d) 110 planes. Overlaid on the fluorescence images are the surface crystallographic orientations oriented as described in the text. The images are 1.58 mm × 1.58 mm, and the intensity is represented by a color, indicated in the calibration bar.

NaCl (ACS grade), pH = 7.5 (±0.05) adjusted with HCl in a sealed microcentifuge tube for 1.0 h. The modified electrode was taken out and rinsed with the solvent buffer solution followed by water. Following the MCH modification, the electrode was immersed in 30 μL of 1.0 μM HS-ssDNA-Alexa488 solution made in an immobilization buffer (10 mM Tris, 100 mM NaCl and 500 mM $MgCl_2$,(Sigma, bioultra) (pH = 7.5 (±0.05) adjusted with HCl) in a sealed microcentrifuge tube for 24 h. After the thiolated DNA treatment, the electrode was stored in the immobilization buffer for 12 h before further characterizations.

Electrochemical Measurements and in Situ Fluorescence Imaging. The modified gold bead electrode was used as a working electrode. The electrochemical measurements were performed with a Pt coil counter electrode and a reference electrode (Ag/AgCl for HS-C10-BODIPY SAM and HS-Aib4-BODIPY SAM and SCE for the MCH-DNA SAM) connected to the working solution via a salt bridge. The working electrolyte solution was 50 mM $KClO_4$ (pH = 12(±0.25) adjusted with KOH) for experiments with the HS-C10-BODIPY SAM and the HS-Aib4-BODIPY SAM. Experiments with the MCH-DNA SAM used a buffer solution with 10 mM Tris and 10 mM KNO_3 (ACS grade), pH = 7.5(±0.05) adjusted with HNO_3. The electrolyte solution was deoxygenated with Ar in all experiments. The fluorescence images were acquired with a EM-CCD Evolve digital camera through a 5× objective (NA = 0.13) producing images that represent 1.58 mm × 1.58 mm regions of the surface. The same filter set was used for BODIPY and Alex488 fluorophores (filters from Chroma, ex:ET470/40X, dichroic:T495LPXR, em:ET520/50M). The images were taken at specific potentials in a spectroelectrochemical cell designed for use on an inverted epi-fluorescence microscope (Olympus IX70) as described elsewhere.[23−26] During imaging, the potential was controlled with a FHI potentiostat coordinated with a LabView program. Fluorescence images (ex: 470 nm, em: 520 nm) were acquired after the potential was changed to the desired value. The starting potential was 0.0 V/AgAgCl, and was changed by −20 mV until −1.3 V/AgAgCl (for the HS-Aib4-BODIPY SAM, each step was 4.0 s long). For the HS-C10-BODIPY SAM, the final potential was −1.4 V (vs AgAgCl) with a 2.0 s wait time at each potential. Fluorescence images (ex: 470 nm, em: 520 nm) were taken at 0 V/SCE and −0.4 V/SCE for the electrode modified with a MCH-DNA SAM. The time sequence for potential step and image acquisition for each measurement is given in the Supporting Information (Figure S2).

RESULTS AND DISCUSSION

Modification of the Au bead surface, and the resulting in situ fluorescence imaging study as a function of the dc potential will be demonstrated for three different types of surface modifications: a fluorophore labeled alkylthiol whose characteristics has been detailed previously,[18,23,24] representing the quintessential type of thiol based SAM; a peptide modified surface representing the biomolecular functionalization of biosensor surfaces; and finally a SAM composed of a mixed monolayer of mercaptohexanol and thiolated DNA representing the popular motif for creating nucleic acid based biosensor surfaces and enabling the study of thiol exchange as a function of surface crystallography.

Analysis of a HS-C10-BODIPY SAM. The study of the influence of surface crystallography on the reductive desorption process of thiol SAMs has been reported.[9,27−33] The reduction of the SAM from the Au(111) surface occurs at the least negative potential in alkaline solution. The 100 and the 110 surfaces follow with increasing negative potential, while the 210 surface has a similar reductive desorption potential as the 110 surface. The differences in the desorption potential (E_{des}) are thought to be due to a combination of the potential of zero charge (pzc) of the surface studied and the strength of the intermolecular interaction.[9] We have used fluorescence imaging and a fluorophore labeled alkylthiol to study this process on polycrystalline bead electrodes for both the reductive and oxidative desorption.[18,23] A fluorescence signal is observed only when the adsorbed molecule becomes desorbed and separated from the electrode surface, decreasing efficiency of the metal-mediated quenching of the luminescence.[26] This approach enabled visualization of the desorption from various parts of the multicrystalline electrode surface when using in situ fluorescence microscopy during electrochemistry. The removal of the SAM from the 111 surface occurred at the least negative potential, with other regions of the surface desorbed at more negative E_{des}.[18] This fact is relied upon in this work for identifying the surface features on the single crystalline gold bead electrode imaged in the in situ experiments.

Figure 1a shows an optical image looking up at the bottom of the Au bead used. Four large facets are observed in the corners of the image (outlined) in addition to a circular defect (upper middle of image) created during the cooling process. The facets are 111 surfaces which are the predominant flat features used in orientation for making polished single crystal electrodes.[1,2] These facets are more clearly observed in the fluorescence images taken during the reductive desorption of HS-C10-BODIPY SAM from the electrode bead surface (Figure 1b−d). The fluorescence intensity is false colored and scaled logaritmically due to the large changes in intensity. The first increase in fluorescence was observed at −1.17 V/AgAgCl coming from the four 111 facets, symmetrically oriented with respect to the center of the image, appearing at the four corners

DOI: 10.1021/ja5104475
J. Am. Chem. Soc. 2015, 137, 276−288

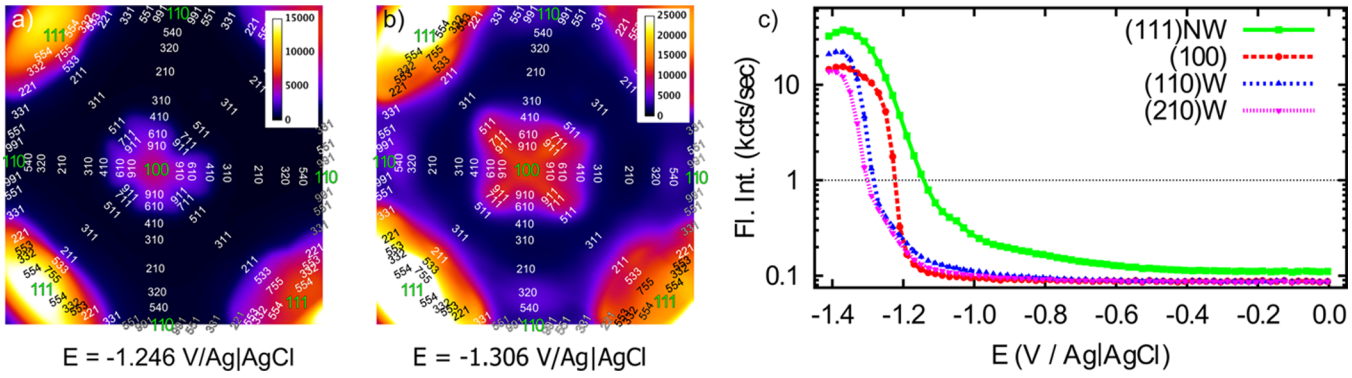

Figure 2. Fluorescence image of the bead electrode (a) −1.25 V/AgAgCl and (b) −1.31 V/AgAgCl with overlay of stereographic triangle showing the low index and vicinal surfaces. The images are 1.58 mm × 1.58 mm, and the intensity is represented by a color, indicated in the calibration bar. (c) Fluorescence intensity as a function of potential for four surfaces (111, 100, 110, 210).

of the image. These areas are coincident with the facets observed in the brightfield images. Further negative in potential (−1.25 V/AgAgCl) fluorescence is observed from the center of the image, revealing a 4-fold symmetric cross, with each arm of the cross directed in between the 111 facets (the presence of the defect results in a distortion of the NE portion of the cross). Both the position with respect to the 111 facets and the desorption potential indicate that this 4-fold symmetric feature is due to desorption from the 100 surface. Applying more negative potentials (−1.31 V/AgAgCl in Figure 1d) reveal that the regions between the 111 facets begin to fluoresce, which indicates a surface with a more open structure, such as 110 or 210.

The images present a highly symmetric potential dependent behavior suggesting that the bead is indeed single crystalline in nature. The 111 facets are oriented in a 4-fold symmetric fashion around the 100 surface, in accordance with a crystallographic projection. In addition, in between each 111 facet, the 110 surface are present, again oriented in a 4-fold fashion around the 100 surface, shifted by 45° with respect to the 111 facets. These patterns and relationships are well-known, being observed in the 1940s for oxidation of Cu single crystal beads[34] and observed on Pt bead single crystals that were flame annealed enhancing the facets.[2] The electrode surface resembles a stereographic projection centered about 100, though it must be pointed out that the stereographic projections typically seen in textbooks[35] cannot be used as a map for this image. The electrode surface is imaged from directly below so the surface features will be projected onto the image plane rather than what is usually done with stereographic projections[1,35] (a comparison is schematically depicted in Figure S4). Since the 100 surface shown in Figure 1 is not exactly at a position that is at the bottom of the electrode surface (closest to the optical window), small adjustments have to made in the projection so as to compensate. The optimal mapping is found by rotating around the *x*- and *y*-axes (in plane of the page) and the *z*-axis (out of the page). As shown in Figure 1 for the low index surfaces, and reproduced in Figure 2 for the higher index vicinal planes, the calculated stereographic map is overlaid on the fluorescence image acquired at −1.25 V/AgAgCl. The 111 facets and 100 region correspond to the positions expected. This allows for the 110 and 210 surfaces to be accurately located as well as the stereographic triangles for each quadrant. The almost perfect symmetry of the fluorescence image and the excellent correlation with the mapping procedure for all quadrants on the surface demonstrates the single crystal nature of the Au bead. The displayed symmetry about the 100 spot is essential for further indepth analysis of the influence of a wide variety of surface structures on the nature of the SAM.

A plot of the potential-fluorescence intensity for the three low index surfaces is shown in Figure 2 (taken from the WNW stereographic triangle, but very similar results are obtained from all other triangles shown in Figure S5). The potential at the start of desorption was determined by using a threshold of the fluorescence intensity (e.g., 1000 cnts/sec), which represents the largest increase in fluorescence. The desorption order in potential is 111 > 100 > 110 > 210 demonstrating the expected ordering of desorption for alkylthiols.[9,10] Furthermore, the intensity of the fluorescence measured can be roughly correlated with the number of molecules desorbed from the surface. In this analysis, it is important to note that the desorbed molecules, which diffuse away from the electrode slowly[18,23,24] will contribute to the observed intensity even after the electrochemical desorption process is complete. These desorbed molecules not only will fluoresce in the same region where they originated, but also can drift to other regions at more negative potentials, complicating the intensity measurement. Nevertheless, for moderately negative potentials an indication of the extent of adsorption coverage can be determined. The 111 facets are 2−3× more intense than the 100 facet which is slightly less than the 110 region but similar to the 210 region. It is important to remember that the surface modification was done rather quickly (15 min) as compared to the usual long immersion time for alkylthiol SAMs in addition to the fact that the BODIPY fluorophore label can also act to induce steric influences on the packing density. The short assembly time was found to produce a high contrast in the fluorescence images between the various surface features and can be considered as characteristic of the initial adsorbed layer before the annealing step which requires many hours.[36] Further measurements were performed on a 18 h annealed sample using the same bead, showing the same relative potential dependence for desorption of the various surfaces but slightly shifted negative in potential (data shown in Figure S6). Interestingly, the intensities measured are very similar to the short exposure samples confirming the belief that the two stage adsorption process occurs in which fast adsorption is followed by an annealing process that may only slightly increase the coverage.[36]

With this mapping, the reductive desorption behavior as a function of potential can be ascertained for any crystallographic

DOI: 10.1021/ja5104475
J. Am. Chem. Soc. 2015, 137, 276−288

Table 1. Miller Indices of Some of the Surfaces Explored in This Work along with the Corresponding Step Notation

100−111	step notation	110−111	step notation	100−110	step notation
100		110		100	
911	5(100) × 111	991	5(110) × 111	610	6(100) × 110
711	4(100) × 111	771	4(110) × 111	510	5(100) × 110
511	3(100) × 111	551	3(110) × 111	410	4(100) × 110
311	2(100) × 111	331	2(110) × 111	310	3(100) × 110
311	2(111) × 100	331	3(111) × 111	210	2(100) × 110
211	3(111) × 100	221	4(111) × 111	210	2(110) × 100
533	4(111) × 100	553	5(111) × 111	320	3(110) × 100
322	5(111) × 100	332	6(111) × 111	430	4(110) × 100
755	6(111) × 100	554	10(111) × 111	540	5(110) × 100
111		111		110	

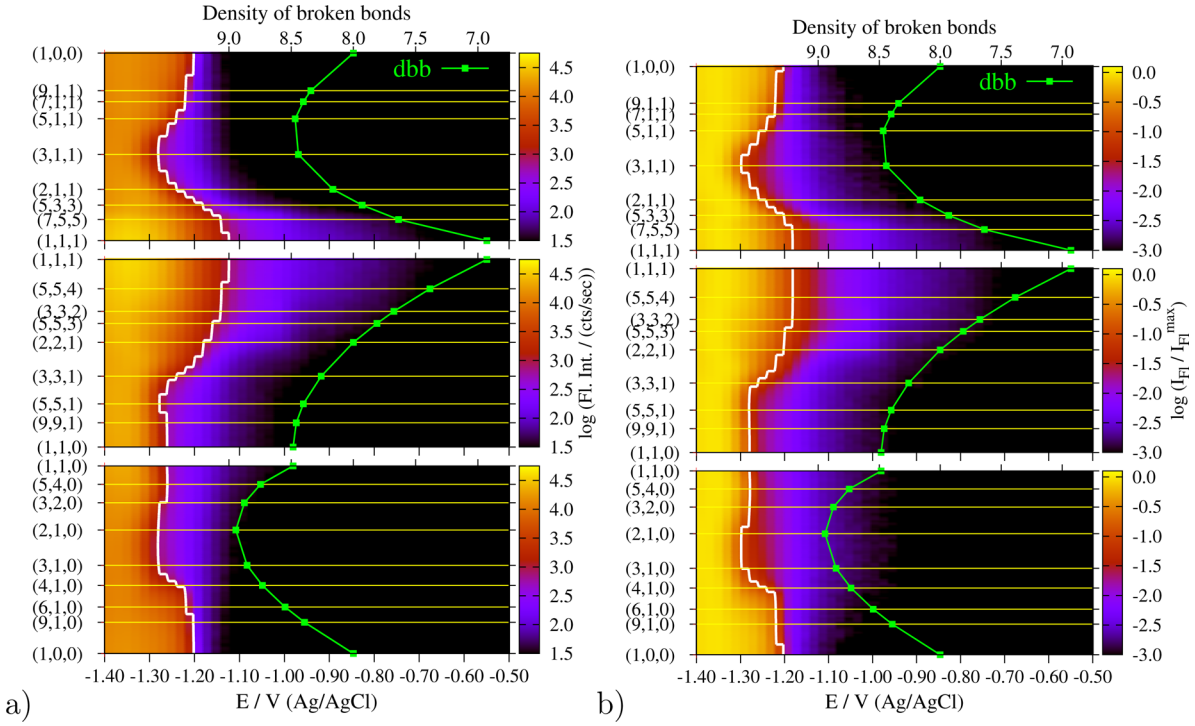

Figure 3. Influence of surface crystallography on the fluorescence intensity changes with potential shown for the 100−111, 111−110 and 110−100 zone axes. The false color represents fluorescence intensities (shown using a log scale). (a) Raw fluorescence intensity with a contour line (white) drawn at an intensity of 1000 cts/sec, similar to the dotted line in Figure 2. (b) The false color represents the log of the ratio of the fluorescence intensity to the maximum intensity for each pixel along the zone axes; the contour line is drawn at 10% of the maximum intensity. In both figures, the density of broken bonds calculated for each surface on the *y*-axis is included.

orientation enabling the analysis of the dependence of the desorption potential and therefore adsorption energy on surface structure. When progressing along the three zone axes (100 to 111, 111 to 110, 110 to 100), the surface is considered stepped with systematic changes in the step density. Moving from one low index plane to another along these zone axes represents changes in the nature of the terrace and the step edge. This is most easily recognized in the step notation introduced by Somorjai[37] where the size and crystallography of the terrace is given, along with that for the step. Shown in Table 1 are both the Miller and step notations for the vicinal surfaces highlighted in this work.

Given that these surface features are all represented on the electrode surface and are imaged as a function of potential, the changes in fluorescence intensity can be plotted as a function of the crystallographic orientation along each side of the crystallographic triangle. These line scans along the zone axes, or crystallography−potential plots are shown in Figure 3 for 100−111−110−100 zone axes outlined in Figure 2 starting from the center, exploring the lower part of the upper left quadrant (aka the west-northwest (WNW) half quadrant). For a single crystalline bead, the same type of plots should be observed for each stereographic triangle (a total of eight can be realized in the measurements performed, selected data shown in Supporting Information, Figure S7). The data are presented as images of the log of intensity (due to the large changes in fluorescence intensity) as a function of the potential and surface crystallography. Also shown is the calculated density of broken bonds (dbb) for the surfaces indicated.[38] The dbb is the number of broken nearest neighbor (Au−Au) bonds per unit surface cell (normalized by the surface cell area) which results from creating a surface and is closely correlated with the work function for that surface. For a fcc crystal, the dbb is a minimum for 111 (6.9) and maximum for 210 (8.9). It is also correlated

DOI: 10.1021/ja5104475
J. Am. Chem. Soc. 2015, 137, 276−288

to the potential of zero charge (pzc)[8,38] for a gold-electrolyte interface (in the absence of adsorbates) and this close correspondence contributes to the analysis of the desorption potential (E_{des}) and its dependence on surface crystallography and its surface energy. A comparison of the potentials at which reductive desorption begins can be obtained by defining a threshold intensity. In Figure 3a, a contour line is drawn at an intensity of 1000 cnts/sec over baseline noise (after subtracting the minimum intensity) while in Figure 3b the threshold is drawn where the intensity exceeds 10% of the maximum fluorescence intensity for that spot on the surface. Similar profiles are obtained for both analysis methods.

Reductive desorption potentials (E_{des}) show some strong changes with surface crystallography. Along the 100−111 zone axis (top panels in Figure 3), the most negative E_{des} is observed for the 311 surface. The 311 surface is characterized as either 2(100) × 111 or 2(111) × 100 in the step notation and represents the transition from 100 terraces to 111 terraces. The step is 2 atoms wide and seems to coordinate the alkylthiol most strongly, suggesting an adsorption site that may involve many gold atoms. The 311 surface has a large dbb, but the desorption potential does not follow the dbb closely in this zone, confirming that the energetics of desorption are controlled by more than the pzc (or dbb). Intermolecular interactions and packing density were found to be important.[9]

The 111 to 110 zone axis shows large changes as well, with the reductive desorption potential remaining at the 111 value (due to the large area occupied by the 111 facet) dcreasing to more negative potentials (characteristic of 110) at 331 then remaining constant. In contrast, the smoothly changing dbb constantly increases from 111 to 110 and appears to be only representative of the fluorescence changes at the low index positions, not the vicinal surfaces in between. The 331 surface is the turning point of the zone where the terraces change from 111 to 110 (2(110) × 111 or 3(111) × 111). The constant E_{des} from 331 to 110 can be understood as the 110 surface dominating the behavior of the alkylthiol adsorption. The slow increase in E_{des} from 331 to 111 suggests that the increase in the 111 terrace width is accompanied by an increase in the 111 adsorption character.

A similar observation is found for the 100−110 zone axis, with the most negative E_{des} observed around 210, as expected. The desorption potential increases at 310 (toward 100) and 320 (toward 110). The change in the dbb also follows this trend showing a maximum at 210. Again the 210 surface represents the transition from 100 to 110 terraces (2(100) × 110 or 2(110) × 100) and is considered as one of the most atomically open surfaces. For this zone axis, the E_{des} follows the change in the dbb or pzc.

These examples show that the smoothly changing dbb or pzc for the Au surface is not a proxy for estimating reductive desorption potentials for those surfaces that are not low index planes. A general trend emerges, that the surface with the more negative E_{des} is correlated with an increase in the step/terrace atom ratio, becoming significant at surfaces that represent a transition between low index planes. This suggests these surfaces offer a more stable environment for the alkylthiols due to increased interaction with the substrate atoms and possibly an increase in intermolecular interaction due to optimized orientation or molecular tilt angles. Both would tend to make E_{des} more negative indicating that more energy is required for desorption. A closer examination of these surfaces using methods that report on molecular orientation or structure is required to address the specific nature of the intermolecular interaction and the specific adsorption site. The approach described above provides direction to these studies with trends in the coverage and energetics of the surface−adsorbate interactions.

The assembly of alkylthiols on gold is most often studied on the low index planes. Adsorption onto 111 and 100 surfaces were found to adopt a $(\sqrt{3} \times \sqrt{3})$R30° and c(2 × 2) surface mesh, respectively.[14] Theoretical calculations of the adsorption energy of methanethiol onto low index planes reported fcc hollow, 4-fold hollow and step-edge for the 111, 100, 110 surfaces, respectively.[39] Other studies highlight the importance of the substrate-S interaction in particular when considering higher index surfaces.[40,41] The introduction of steps would change the specific interaction with the surface and between adsorbates. The adsorption of alkylthiols onto stepped surfaces has been infrequently studied experimentally, but theoretical calculations indicate that in the limit of a small adsorbate (MeS), adsorption typically occurs on 2-fold or bridge sites on the stepped surfaces examined.[42] The differences in the adsorption energy are in-line with the desorption potentials measured here given that the resolution of binding energies are ∼0.03 eV in a vacuum. For the 111, 100, and 110 surfaces, bridge sites are favored over on top sites with adsorption energies ordered as expected from the desorption images 110(−0.71 eV) > 100(−0.57 eV) > 111(−0.15 eV). For the 310, 210, 320 surfaces, bridge sites are again favored, all showing small changes in adsorption energies (∼−0.6, −0.55, −0.51 eV respectively). For the 311−211−322 surfaces, bridge sites are favored all showing similar adsorption energies (∼−0.75 to −0.8 eV). We find that the molecules adsorbed onto the 311 surface requires the most negative E_{des} for this zone, in fact as the size of the 111 terrace increases (211 to 533 to 322−322 is between 755 and 533), the E_{des} becomes less negative in contrast to the calculations. The 331−221−332 path also show lowest adsorption energies for bridge sites with similar adsorption energies (−0.72, −0.68, −0.64 eV respectively). These calculations are done in vacuum and for the shortest alkylthiol, thereby not considering the influence of electrolyte or intermolecular interactions in the adsorption energies. The low index planes show the correct ordering, but the vicinal surfaces are less convincing confirming the complex interactions at the steps.

The self-assembly of alkylthiols onto gold shows an influence of the pzc (or dbb) and intermolecular interaction on the energetics of desorption. To demonstrate that the measurements made on these single crystal gold bead electrodes are indeed strongly influenced by the surface crystallography, the same analysis was performed on a SAM created from fluorophore labeled Aib peptides. Thiolated Aib peptide form helical structures and maintain helicity when in a SAM due to the strong intramolecular hydrogen bonding; they occupy a larger footprint than the alkylthiols. The Aib peptide also has a strong dipole directed along the helix. This SAM will have different intermolecular interaction characteristics (H-bonds)[43−47] as compared to the alkylthiol, which should result in a significant difference in the adsorption as a function of surface crystallography.

Analysis of the Aib Peptide (HS-Aib4-BODIPY) SAM. The modification of metal surfaces, either as planar electrodes or nanoparticles by thiolated Aib peptide SAMs has been reported.[43−47] Because of the steric hindrance associated with the Aib residue, Aib peptides form 3_{10}-helices induced by

DOI: 10.1021/ja5104475
J. Am. Chem. Soc. 2015, 137, 276−288

intramolecular C═O···H—N hydrogen bonds between residues i and i + 3. The highly sterically constrained conformation of Aib peptides and the orientation of its polar group induce a strong dipole moment along peptide backbone. In this work, a thiolated Aib peptide characterized by 3 intramolecular hydrogen bonds, thiolated at the N terminus, dipole directed from C to N terminus was used to form SAMs surface, the dipole moment oriented in this way allows forming particularly stable SAMs. The maximum apparent packing density of this peptide SAM was calculated to be ~3 × 10^{14} molecules·cm^{-2} (0.33 nm^2/molecule) by cyclic voltammetry desorption experiments.[47] This area per molecule is smaller than the calculated footprint of the helix, estimated at ~0.8 nm^2/molecule[45] which suggests that the simple charge integration of the reductive desorption current may not be accurate for SAMs with large dipole moments. FTIR reflection absorption measurements indicated that the peptide molecules form a rigid network through intermolecular hydrogen bonds, which accounts for a highly ordered and stable monolayer on well prepared planar gold substrates[47] as well as on monolayer protected Au nanoclusters.[43,44,46] Reductive desorption was found to occur at −0.91 V/AgAgCl for these well packed SAMs. The adsorption onto Au surfaces other than 111 have not been electrochemically characterized.

Modification of a separate single crystal Au bead by a thiolated Aib peptide, labeled with the same BODIPY fluorophore as the alkylthiol discussed above, was performed and its reductive desorption character studied as a function of the surface structure. The desorption of HS-Aib4-BODIPY from different facets follows a similar sequence to that observed for the alkanethiol except occurring at less negative potentials. The intensity variation with potential for specific crystallographic regions are shown in Figure 4 along with the

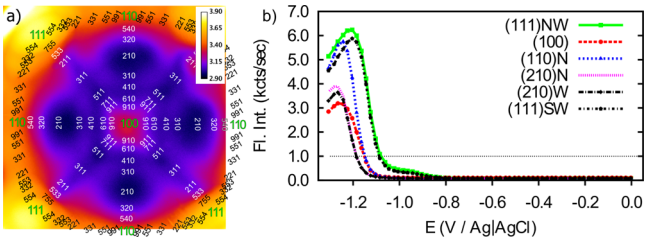

Figure 4. Reductive desorption of a HS-Aib4-BODIPY peptide SAM on the Au bead. (a) A fluorescence image captured at −1.184 V/AgAgCl showing the extent of Aib-peptide SAM reductive desorption and its crystallinity dependence. The fluorescence intensity is log scaled to enhance the contrast. (b) The intensity variation with potential for the (111) facets and other surface regions are shown.

crystallographic map of the electrode surface. The 111 facets desorb at the least negative potential, but in this case with a two step desorption, first at −0.8 V/AgAgCl and finally at −1.1 V/AgAgCl. The nature of this two step reductive desorption is not clear, but does depend on the concentration of the peptide in the deposition solution. When studying the same molecule as a SAM on Hg, Beccuci et al.[45] suggested that the desorption of the Aib peptide SAM is accomplished in two steps, the breaking of the Hg−S bond, then displacement of the thiolate from the Hg surface with solvent. Since the Aib peptide modified with BODIPY is sparingly soluble in the electrolyte used, the two step desorption we observe via fluorescence may be evidence of this two step process: the Au−S bond breaking at −0.8 V/AgAgCl and the molecule separating from the surface at −1.1 V/AgAgCl becoming more fluorescent due to the decrease in quenching efficiency. The advantage that these single crystalline beads measurements provide is the ability to observe that this two step desorption is only observed on the 111 facet (also observed on large single crystalline 111 electrodes) but not observed for any other crystallographic orientation. Reductive desorption initiates on the 100 and 110 surfaces at −1.18 V/AgAgCl, with desorption from the 210 surface starting at −1.20 V/AgAgCl. These layers were created from a dilute solution of the HS-Aib4-BODIPY peptide over a short period of time (2 h), resulting in a layer that may not be as well organized as previous experiments on extended gold surfaces observed in the literature[47] also considering the large BODIPY moiety attached (BODIPY is roughly as wide as the diameter of the helix). The fluorescence intensities are much lower than for the alykthiol SAM, suggesting a low surface coverage. In this low coverage case, it might be assumed that the intermolecular interactions may not play such a significant role in influencing the E_{des}. Interestingly, the coverage on the 111 and 110 planes are roughly double that on 100 and 210 surfaces possibly reflecting the initial stages of the adsorption process as dependent on the coordination with the surface.

Using the same strategy as for the alkylthiol, the surface was indexed to include the vicinal surfaces between the low index planes overlaid onto the fluorescence image captured at −1.184 V/AgAgCl in Figure 4. The symmetry of the fluorescence image clearly shows the single crystal character of the electrode surface with the intensity differences observed reflected in the four quadrants equally (exception is the small defect in the NE quadrant (upper right) around the 211 label, this is a dimple in the surface that forms during cooling). The differences in intensity at this potential are significant with a clear minimum along the 100−111 zone axis, and a significant minimum at the 210 spot. The contrast observed in the fluorescence images are characteristic of the particular potential chosen revealing different surface features.

The fluorescence intensity as a function of potential and surface crystallography are shown for the fcc stereographic triangle in Figure 5a using a threshold of 1000 cnts/s or in Figure 5b using a threshold of 10% of the maximum intensity to compensate for the differences in the coverage. The change in the intensity with crystallography is again compared to the dbb as a surrogate for the pzc. The changes in desorption potential along the 100−111 zone axis show a good correspondence with the dbb with the most negative desorption potentials observed from 511−211 corresponding to the largest dbb values for this axis. The two step desorption for the 111 surface is visible and extends out to 755, which may be due to the size of the facet intruding on the ideal surface orientation assignment. The 111−110 zone axis also shows this two step desorption, but over a much larger range of surfaces, suggesting that the size of the facet may not be the only factor. E_{des} becomes more negative at the 553 surface, remaining constant at the 331 surface, the turning point for this zone. These changes also broadly agree with the trend in the dbb. The 110−100 zone axis shows the most negative desorption potential for 210 or 310 surfaces, roughly in line with the dbb, but shifted toward surfaces with more 100 character. Interestingly the 210 region does not have the most negative desorption potential (511 to 311) even though it has the largest dbb.

The characteristics of the crystallographic influence on the reductive desorption of the HS-Aib4-BODIPY SAM are very

DOI: 10.1021/ja5104475
J. Am. Chem. Soc. 2015, 137, 276−288

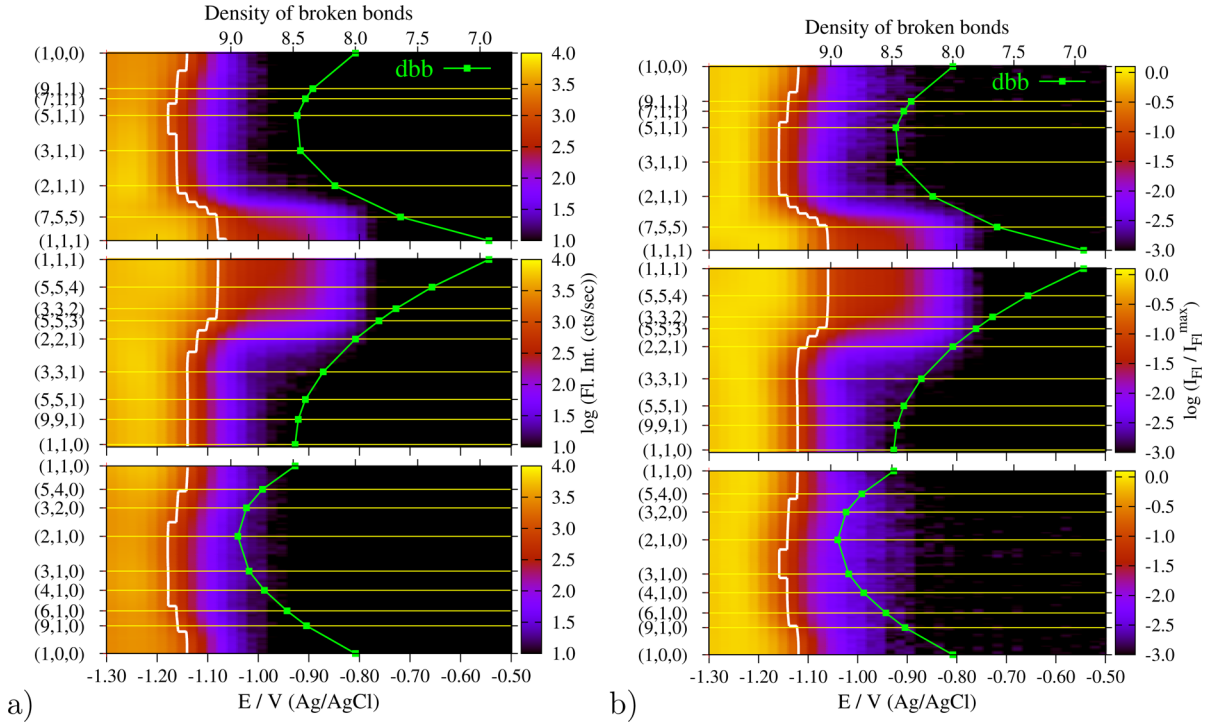

Figure 5. Influence of surface crystallography on the fluorescence intensity changes with potential shown for the 100−111, 111−110 and 110−100 zone axes. The false color represents fluorescence intensities (shown using a log scale). (a) Raw fluorescence intensity with a contour line drawn at an intensity of 1000 cts/sec, similar to the line drawn in Figure 4. (b) The false color represents the log of the ratio of the fluorescence intensity to the maximum intensity for each pixel along the zone axes; the contour line (white) is drawn at 10% of the maximum intensity. In both figures, the density of broken bonds calculated for each surface on the *y*-axis is included.

different than those observed for the alkylthiol. The reductive desorption potential seems to follow the dbb or pzc more closely than the alkylthiol, suggesting that the intermolecular interactions may not be as strong as the hydrophobic interactions in the alkylthiol case. This helical Aib peptide has a large footprint, a large dipole and lower coverage as compared to the alkylthiol SAM which tends to lessens the SAM stability due to the less energetic intermolecular interactions, generally evident by the less negative reduction potential, but now specifically indicated for many surfaces. Comparing these two distinct types of SAMs shows the utility of the fluorescence imaging approach used on these Au single crystal electrodes in revealing the influence of surface crystallography in a self-consistent and comparable fashion.

Estimating E_{des} of Alkylthiol and Aib SAMs as a Function of Surface Crystallography. The influence of surface crystallography on the reductive desorption potentials for the two SAMs can be compared by interpolating the value of the potential (E_{des}) at which the fluorescence intensity crosses a threshold. This was done for each pixel in the fluorescence images for both SAMs using either 1000 cnt/s or 10% of the maximum fluorescence intensity (for that particular pixel) as the thresholds. The results are shown in Figure 6 for the HS-C10-BODIPY SAM (Figure 6a,b) and the HS-Aib4-BODIPY SAM (Figure 6c,d) respectfully. Both absolute and relative thresholds provide very similar information, the 10% of maximum intensity showing less influence of the surface coverage, even though coverage can also influence desorption potential. In addition, the dbb for a fcc surface was calculated with the same orientation and projection as the fluorescence images (i.e., centered at 100) with color coding to match the desorption potential trend, facilitating a direct comparison (Figure 6e). As expected the dbb is largest at the 210 (dark) and smallest at the 111 surface (light). The dependence on surface crystallography is clearly different for both systems, even though the low index and 210 surfaces are similarly ordered. As the images represent a complete stereographic triangle, analysis can provide significant insights into the influence of crystallographic orientation. The alkylthiol SAM E_{des} map shows that the region around 100 (composed of surfaces that have large 100 terraces like 910, 610) displays a cross shaped pattern where E_{des} is similar to the 100 surface. This indicates that surfaces where the step edges (110) are separated by 100 terraces which are greater than five atoms wide have little to no influence on E_{des}. As expected, the 210 surface for the alkylthiol SAM shows the most negative E_{des}, which is also true for the regions all around the 100 surface. The dbb decreases when moving from 210 to either zone axis, which suggests a less negative desorption potential, but this is not observed in the E_{des}map. The specific intermolecular interactions characteristic of the alkylthiols influence E_{des} so that the trend in the reductive desorption potential is not completely predictive using the dbb or pzc for surfaces other than the low index planes.

Desorption of the Aib peptide SAM in the vicinity of the 100 surface is symmetrically distributed around the 100 surface (resembling the pattern in the dbb map) indicating that the terrace is dictating the interaction strength. The 210 surface has a more negative E_{des}, which is expected given its most negative pzc. Unexpected is the even more negative E_{des} that is observed for the 100−111 zone axis. These surfaces (911 to 211) have 100 terraces with an increasing density of 111 steps (at 311 the steps and terraces are equivalent). The HS-Aib4-BODIPY SAM desorbs at a more negative potential than even the 210 surface

DOI: 10.1021/ja5104475
J. Am. Chem. Soc. 2015, 137, 276−288

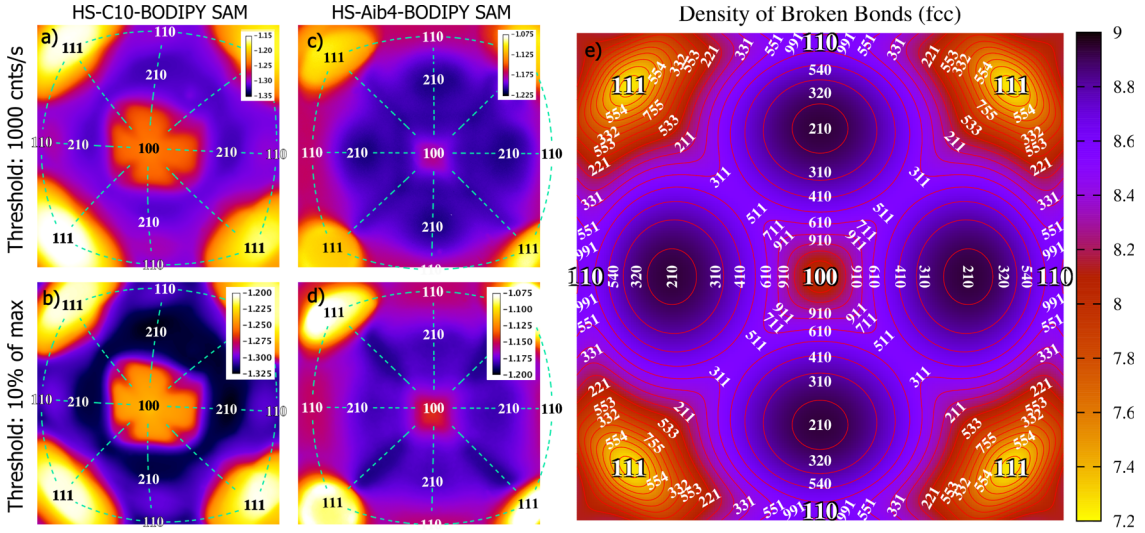

Figure 6. A map of the interpolated reductive desorption potential (E_{des} vs AgAgCl) for the alkylthiol HS-C10-BODIPY SAM (left column) and the HS-Aib4-BODIPY SAM (middle column) using a threshold of 1000 cnts/sec or a 10% threshold. The image on the right is the calculated density of broken bonds (dbb) for a fcc spherical surface observed from the bottom with the 100 surface in the center.

for these vicinal surfaces. This reveals that the 111 step coordinates with HS-Aib4-BODIPY strongly, which may be enhanced with intermolecular dipolar interactions (remember this layer is made purposefully low coverage so as to reveal the initial state of the SAM). The pzc for these surfaces (711 to 311) are somewhat comparable to each other but are not at the extreme value of the 210 surface. This illustrates a discrepancy when comparing E_{des} and dbb trends across different zone axes. This type of comparison represents a useful starting point for further in-depth molecular study of adsorbates on these vicinal surfaces to understand these differences. The majority of experimental studies have focused on low index planes for which the SAMs formed from these two adsorbates show very similar trends. For our results it is clear that the two adsorbates show a very different dependence of E_{des} on the surface crystallography when considering more open surfaces which must be due to differences in the nature of the adsorbed monolayer, its coordination with the surface, surface coverage and intermolecular interactions (e.g., hydrophobic and/or dipolar type interactions). The use of a single crystal Au bead and the in situ imaging approach can guide the more detailed study of the adsorption onto the unusual and understudied surface crystallographies.

The assignment of surface crystallography used in this method for interrogating such surface−adsorbate interactions is dependent on the absence of surface relaxation, which is typically observed in electrochemical systems,[4,8] but usually at positive potentials and in the presence of ionic or molecular adsorbates. The negative potentials used in this work puts the analysis in the unreconstructed domains for most if not all surfaces. For example, the Au(100) surface is known to reconstruct at +0.2 V/SSCE (in H_2SO_4), but this is lifted at −0.220 V/SSCE.[4] This is one of the most negative potentials for the lifting of the reconstruction and is still far positive of the potentials used in this work. Even so, the electrodes are not polarized during the formation of the SAMs and therefore could still be reconstructed when performing the reductive desorption. In this work, we will assume the surfaces are not reconstructed. Another issue is that the presence of large terraces (111 in particular) clouds the interpretation of the surfaces near 111 and may result in an inaccurate map around the edges of these facets. These effects are not expected to be large because these regions probably behave much like the facet and therefore, may not contribute much to our understanding of the surface crystallographic influence on the molecule−substrate interaction. It is also important to point out the use of the dbb as a surrogate for surface energy can only apply to the Au-electrolyte interface. The presence of a SAM has been shown to substantially negatively shift the pzc for alkylthiol SAMs on Au(111).[48,49]

This experimental approach enables the interrogation of more complex systems, multicomponent or multiple step surface modification routines as the surface modification and the analysis are performed with exactly the same conditions, something that can be quite challenging to achieve within a set of polished single crystal surfaces. We demonstrate this advantage on a complex multistep competitive adsorption surface modification using MCH and ssDNA mixed SAMs.

Examining the Extent of Thiol Exchange via Surface Specific Studies of a Mixed SAM of MCH-ssDNA. The preparation of DNA SAMs on gold has been studied for more than 10 years.[50−52] The standard approach to making these surfaces is to first expose thiol modified ssDNA to a typically clean polished polycrystalline gold surface for 24 h, then after washing, immerse in a short alkylthiol like mercaptohexanol (MCH) to displace the nonspecifically adsorbed DNA, and to passivate the metal surface.[53−57] We have studied these systems and found the surfaces to be less than ideal pictures of uniform monolayer of DNA with evidence of multilayer formations on the electrode surface.[25] Reversing the SAM preparation steps and requiring the DNA to replace the MCH resulted in lower DNA surface coverage, but preferential adsorption onto various regions of the poly crystalline gold surface was observed. Below, we detail the study of a competitive displacement of the short alkylthiol molecule (MCH) from the gold surface with a thiolated ssDNA molecule. Competitive displacement is often used in the exchange of ligands on gold nanoparticle surfaces.[58−61]

In this example, the single crystal gold bead was modified with MCH. The MCH-DNA SAM was created by partial

DOI: 10.1021/ja5104475
J. Am. Chem. Soc. 2015, 137, 276−288

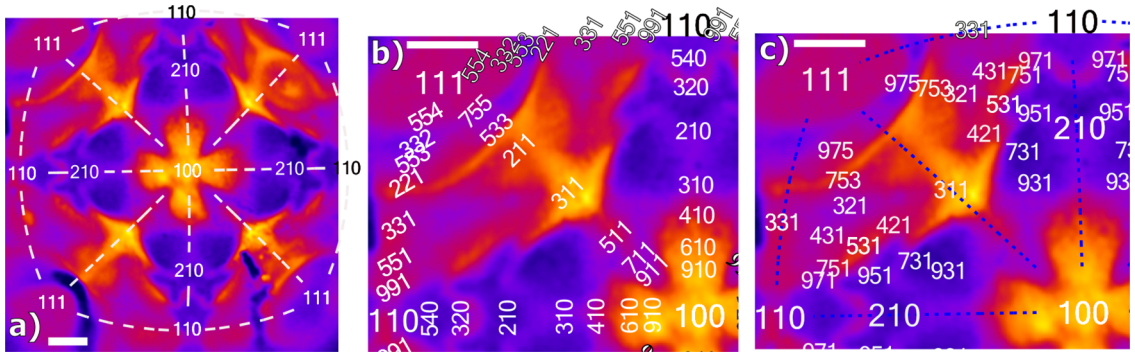

Figure 7. Fluorescence image of a MCH/ssDNA SAM on a single crystal Au bead electrode captured at −0.4 V/SCE indexed with (a) the low index planes shown for the full image with four quadrants, (b) vicinal surfaces along the stereographic zone axes for the NW quadrant and (c) higher index kink stepped surfaces for the NW quadrant. Scale bar in each image is 200 μm.

replacement of the MCH SAM with a 30 base pair single stranded DNA molecule modified with hexanethiol on one end and a fluorophore at the other end, positioning it ∼10 nm away from the thiol. So unlike the HS-C10-BODIPY and the HS-Aib4-BODIPY, the fluorescence is no longer efficiently quenched due to the length of DNA and so fluorescence can be measured at potentials where the SAM is still adsorbed. At moderate negative potentials (not negative enough to reductively desorb the layer), the DNA is repelled from the electrode surface,[53,56] and the fluorophore is further from the surface than in the other two examples. Shown in Figure 7 is a fluorescence image at −0.4 V/SCE of a MCH/ssDNA SAM. The intensity of the fluorescence can be considered as representing the amount of ssDNA that successfully displaced the MCH to become specifically adsorbed onto the surface. There is a clear and substantial influence of the surface crystallography on this competitive displacement process. Moreover, the symmetry displayed is exemplary demonstrating again that the surface is indeed a single crystal, showing 4-fold symmetry as expected for the 100 surface being at the center of the image. The location of the 100 and 111 regions on this Au bead electrode were conformed with a separate reductive desorption imaging experiment using the alkylthiol SAM. This is the same bead that was used for the Aib peptide study described above showing the same defect in the NE quadrant. The Au bead surface surface was indexed and the result is shown in Figure 7 for the (a) low index, (b) vicinal and (c) kinked stepped surface, respectively.

It is important to note that the thiolated ssDNA used is modified by an hexanethiol linker resulting in similar type of intermolecular interaction as the MCH initially adsorbed onto the electrode surface. The extent of DNA adsorption can be estimated through measurements of the fluorescence intensity and compared to the other surface features. This is done for the three zone axes (100−111−110) as well as the kinked stepped surfaces that run from the turning point for each zone axis to the low index plane across from it (210−111, 331−100, 311−110) shown in Figure 8a−f.

The 100 surface has a large fluorescence signal and therefore a high coverage of DNA as compared to the 111 surface, indicating that the MCH SAM is more strongly bound to the 111 surface. The 110 region has a lower intensity as compared to the 111 facet, suggesting that the replacement is not as efficient on atomically rougher surfaces. The structure around the 100 spot is similar to that observed for the alkylthiol, displaying a cross that is more cloverleaf-like in shape rather

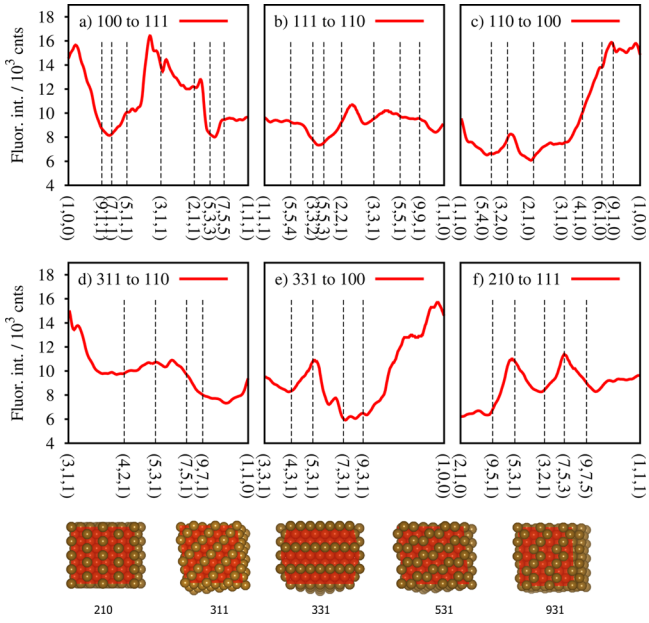

Figure 8. Fluorescence intensity profiles extracted from the indexed fluorescence image taken at −0.4 V/SCE for the MCH-ssDNA surface along the three zone axes (a) 100−111, (b) 111−110, (c) 110−100 and three trajectories from the turning points on the zone axes to the opposite low index plane (pole) (d) 311−110, (e) 331−100, (f) 210−111 from the WNW portion of Figure 7 (bottom) models of some of the surfaces shown in the figures.

than having straight rectangular features. The low intensity regions in between are directed toward the 111 surface, suggesting that the increase in the 111 step density stabilizes the MCH SAM with respect to replacement. The higher intensity 4-fold features are directed toward 110, but only up to 410 (4(100) × 110), the intensity quickly decreasing when the 100 terrace becomes smaller than 4 atoms wide. This is evident for the 210 region which has a lower intensity as compared to the 110, while the region around it has an interesting symmetric structure.

The 311 surface is a particularly interesting feature on the 100−111 zone axis showing the largest fluorescence signal and positioned with 4-fold symmetry about 100 clearly indicating it is not due to surface defects or imperfections. The 311 surface is the turning point for this zone, being equally described as 2(100) × 111 or 2(111) × 100, and represents the atomically rough surface for this zone axis. The extent of MCH

DOI: 10.1021/ja5104475
J. Am. Chem. Soc. 2015, 137, 276−288

replacement is highest here because of a decrease in the MCH adsorption strength at this surface due to a lack of stabilizing intermolecular interactions. It is worth noting that for the longer alkylthiol (HS-C10-BODIPY), the 311 surface had a quite negative desorption potential, which illustrates the influence of intermolecular interactions in the removal or replacement of the adsorbate. Since ssDNA significantly populates this particular region, the adsorption energy for thiolated DNA may be particularly large for the 311 surface, which points to a significant intermolecular interaction between adsorbed DNA or a strong binding to specific atomic surface features. Further work, however, is needed to determine the relative magnitude of these interactions for the 311 surface. Moving from the 311 surface toward the 111 facet, the adsorption of DNA decreases to be midway between 111 and 100 indicating the lessening influence of the 100 step on the extent of exchange.

The possibility also exists for studying the adsorbate exchange characteristics of chiral surfaces which can be found in the regions between the zone axes. Chiral surfaces have been defined depending on the handedness of the kinked edge and are being investigated for their possible specific catalytic activity.[62−67] We have chosen specific trajectories that start from the low index plane to the turning point on the zone axis opposite. The fluorescence intensity along these trajectories are shown in Figure 8d−f. These surfaces have kinked steps which show a varied degree of exchange with the MCH covered surfaces. Two chiral surfaces show interesting behavior. The 531 surface is present in all three trajectories and shows a local increase in the amount of DNA present on the surface for all the intensity−crystallography profiles. The 531 surface is the turning point for all of these trajectories and can be described as having 110 terraces with 311 steps (two other descriptions are also possible). The 311 character of the surface is reflected in the increased DNA coverage which is also evident in 751 and 421. In contrast, the 931 surface (3(100) × 331) has a low DNA coverage, similar to the 210 surface. This cannot be predicted from the 100 or 331 surfaces, which both show significant DNA adsorption. These surfaces are defined as chiral such that the kinked surface on one side of a zone axis is a nonsuperimposable mirror image of the kinked surface on the other side. If the adsorbate−substrate interaction is chiral in nature, some difference would be expected in the fluorescence intensity if the interaction is influenced by the handedness of the kink. In both cases shown here, the analysis shows simple reflection symmetry across these trajectories, suggesting no significant influence of the type of kink on the strength of adsorbate−surface interaction or the extent of the exchange in this case. This approach of fluorescence imaging of a fluorophore labeled SAM assembled onto a single crystal Au bead may thus facilitate the selection of interesting chiral surfaces for further study.

■ CONCLUSIONS

The examination of the influence of surface crystallography on the formation and reductive removal of a SAM was demonstrated for an alkylthiol SAM, a SAM formed by an Aib peptide, and for a mixed SAM formed through thiol exchange between MCH and ssDNA. The use of a single crystal gold bead electrode as the substrate in combination with spectroelectrochemical fluorescence microscopy illustrated the simultaneous study of all surfaces that compose the fcc stereographic triangle. The fluorescence images displayed remarkable symmetry about the central 100 facet, which clearly indicated the single crystal nature of the Au bead substrate facilitating the indexing of the surface. An estimate of the reductive desorption potential for the two single component SAMs showed clear differences in E_{des} for the low index planes, consistent with previous electrochemical studies, but significantly, we were also able to estimate E_{des} for the vicinal surfaces along the zone axes between the most often studied low index planes, as well as the surfaces that are chiral in nature. Comparing the alkylthiol SAM with one created by thiolated Aib peptides illustrated that the influence of intermolecular interactions and molecular coordination to the atomic surface structure both can have large influence on the relative desorption potentials. In both cases, comparison with the density of broken bonds (as a surrogate for the pzc or work function) showed significant differences, especially for the vicinal surfaces. With the large variety of surface crystallography examined, this study confirms the need to consider both the pzc (of the clean and adsorbate covered surfaces) and the strength of intermolecular interactions when explaining E_{des} as a measure of the adsorption energy for these SAMs. We showed that the general trend observed for the low index planes are not necessarily predictive for the more open stepped or kink stepped surfaces. These differences also emphasize the fact that the change in pzc (or work function) due to adsorption or SAM formation may be playing an important role influencing E_{des}.

In addition, the extent of thiol exchange was investigated as a function of surface crystallography for a specific two component SAM. The exchange of adsorbed MCH for thiol modified ssDNA displayed a remarkable dependence on the surface structure, identifying surfaces in which MCH is weakly adsorbed, or the ssDNA is strongly adsorbed. This surface specific thiol exchange study should prove useful in understanding the nature of thiol replacement kinetics and thermodynamics on nanoparticle surfaces. Moreover, we showed that this analysis can easily investigate the differences in the behavior of both types of chiral surfaces, facilitating the study of adsorption onto either chiral surfaces. As the study of the influence of surface crystallography is typically done with many single crystal electrodes and comparative studies rely upon the reproducibility of the formation and analysis of these surfaces, correlating the results can be difficult. The approach presented here, while not able to extract the electrochemical behavior of a single surface, is able to self-consistently study the influence of surface cryatallography for systems that are assembled and then analyzed under exactly the same conditions, facilitating the study of SAM formation and removal over the whole fcc stereographic triangle, identifying potential surfaces for further study.

■ ASSOCIATED CONTENT

Supporting Information

The synthetic procedure for making HS-Aib4-BODIPY is outlined. A schematic of the SAM forming molecules used is provided. The sequence for potential step and image acquistion is also schematically shown. An AFM image of a 111 facet is provided. The projection used for mapping the crystallographic orientation of the bead surface, fluorescence intensity-potential plots for low index planes from other regions on the surface, fluorescence intensity−potential plots for the HS-C10-BODIPY SAM after assembling for 18 h and fluorescence intensity-potential zone axes profiles for other stereographic triangles for the short immersion HS-C10-BODIPY SAMs are

DOI: 10.1021/ja5104475
J. Am. Chem. Soc. 2015, 137, 276−288

provided. This material is available free of charge via the Internet at http://pubs.acs.org.

AUTHOR INFORMATION

Corresponding Author

bizzotto@chem.ubc.ca

Present Address

[||]Institute of Chemistry, Saint Petersburg State University, Saint Petersburg 199034, Russia.

Notes

The authors declare no competing financial interest.

ACKNOWLEDGMENTS

The authors thank Brian Ditchburn (UBC, Chemistry, Glassblowing) for his efforts in creating the spectroelectrochemical cell used in this work. JCM was supported by the National Council of Science and Technology of Mexico (CONACYT) through the scholarship 207929. This research was funded by NSERC (Canada).

REFERENCES

(1) Korzeniewski, C.; Climent, V.; Feliu, J. In *Electroanalytical Chemistry*; Bard, A. J., Zoski, C. G., Eds.; CRC Press: Boca Raton, FL, 2012; pp 75−170.

(2) Komanicky, V.; Fawcett, W. R. *Electrochim. Acta* **2004**, *49*, 1185−1194.

(3) Hamelin, A. *J. Electroanal. Chem.* **1996**, *407*, 1−11.

(4) Silva, A. F.; Martins, A. In *Interfacial Electrochemistry*; Wieckowski, A., Ed.; Oxford University Press: New York, 1996.

(5) Lipkowski, J.; Stolberg, L.; Yang, D.-F.; Pettinger, B.; Mirwald, S.; Henglein, F.; Kolb, D. M. *Electrochim. Acta* **1994**, *39*, 1045−1056.

(6) Stolberg, L.; Lipkowski, J.; Irish, D. E. *J. Electroanal. Chem.* **1987**, *238*, 333−353.

(7) Richer, J.; Lipkowski, J. *J. Electrochem. Soc.* **1986**, *133*, 121.

(8) Hamelin, A.; Martins, A. M. *J. Electroanal. Chem.* **1996**, *407*, 13−21.

(9) Doneux, T.; Steichen, M.; De Rache, A.; Buess-Herman, C. *J. Electroanal. Chem.* **2010**, *649*, 164−170.

(10) Zhong, C. J.; Zak, J.; Porter, M. D. *J. Electroanal. Chem.* **1997**, *421*, 9−13.

(11) Kakiuchi, T.; Usui, H.; Hobara, D.; Yamamoto, M. *Langmuir* **2002**, *18*, 5231−5238.

(12) Vericat, C.; Vela, M.; Benitez, G.; Carro, P.; Salvarezza, R. *Chem. Soc. Rev.* **2010**, *39*, 1805−1834.

(13) Pensa, E.; Cortés, E.; Corthey, G.; Carro, P. *Acc. Chem. Res.* **2012**, *45*, 1183−1192.

(14) Love, J. C.; Estroff, L. A.; Kriebel, J. K.; Nuzzo, R. G.; Whitesides, G. M. *Chem. Rev.* **2005**, *105*, 1103−1169.

(15) Danger, B. R.; Fan, D.; Vivek, J. P.; Burgess, I. J. *ACS Nano* **2012**, *6*, 11018−11026.

(16) Vivek, J. P.; Burgess, I. J. *Langmuir* **2012**, *28*, 5031−5039.

(17) Vivek, J. P.; Burgess, I. J. *Langmuir* **2012**, *28*, 5040−5047.

(18) Shepherd, J. L.; Kell, A.; Chung, E.; Sinclar, C. W.; Workentin, M. S.; Bizzotto, D. *J. Am. Chem. Soc.* **2004**, *126*, 8329−8335.

(19) Voigtländer, B.; Cherepanov, V.; Elsaesser, C.; Linke, U. *Rev. Sci. Instrum.* **2008**, *79*, 033911.

(20) Voigtländer, B.; Linke, U.; Stollwerk, H.; Brona, J. *J. Vac. Sci. Technol., A* **2005**, *23*, 1535.

(21) Clavilier, J.; Faure, R.; Guinet, G.; Durand, R. *J. Electroanal. Chem.* **1980**, *107*, 205−209.

(22) Engelsmann, K.; Lorenz, W. J.; Schmidt, E. *J. Electroanal. Chem. Interfacial Electrochem.* **1980**, *114*, 1−10.

(23) Musgrove, A.; Kell, A.; Bizzotto, D. *Langmuir* **2008**, *24*, 7881−7888.

(24) Casanova-Moreno, J. R.; Bizzotto, D. *Langmuir* **2013**, *29*, 2065−2074.

(25) Murphy, J. N.; Cheng, A. K. H.; Yu, H. Z.; Bizzotto, D. *J. Am. Chem. Soc.* **2009**, *131*, 4042−4050.

(26) Bizzotto, D.; Yang, Y.; Shepherd, J. L.; Stoodley, R.; Agak, J. O.; Stauffer, V.; Lathuilliere, M.; Akhtar, A. S.; Chung, E. *J. Electroanal. Chem.* **2004**, *574*, 167−184.

(27) Thom, I.; Buck, M. *Z. Phys. Chem.* **2008**, *222*, 739−754.

(28) Byloos, M.; Al-Maznai, H.; Morin, M. *J. Phys. Chem. B* **2001**, *105*, 5900−5905.

(29) Wong, S. S.; Porter, M. D. *J. Electroanal. Chem.* **2000**, *485*, 135−143.

(30) Byloos, M.; Al-Maznai, H.; Morin, M. *J. Phys. Chem. B* **1999**, *103*, 6554−6561.

(31) Yang, D.-F.; Wilde, C. P.; Morin, M. *Langmuir* **1996**, *12*, 6570−6577.

(32) Walczak, M. M.; Popenoe, D. D.; Deinhammer, R. S.; Lamp, B. D.; Chung, C.; Porter, M. D. *Langmuir* **1991**, *7*, 2687−2693.

(33) Widrig, C. A.; Chung, C.; Porter, M. D. *J. Electroanal. Chem.* **1991**, *310*, 335−359.

(34) Gwathmey, A. T.; Benton, A. F. *J. Chem. Phys.* **1940**, *8*, 431.

(35) Hermann, K. *Crystallography and Surface Structure; An Introduction for Surface Scientists and Nanoscientists*; Wiley-VCH Verlag GmbH & Co. KGaA: Weinheim, Germany, 2011.

(36) Qu, D.; Morin, M. *J. Electroanal. Chem.* **2001**, *517*, 45−53.

(37) Van Hove, M. A.; Somorjai, G. A. *Surf. Sci.* **1980**, *92*, 489−518.

(38) De Levie, R. *J. Electroanal. Chem.* **1990**, *280*, 179−183.

(39) Masens, C.; Ford, M. J.; Cortie, M. B. *Surf. Sci.* **2005**, *580*, 19−29.

(40) Vericat, C.; Benitez, G. A.; Grumelli, D. E.; Vela, M. E.; Salvarezza, R. C. *J. Phys.: Condens. Matter* **2008**, *20*, 184004.

(41) Cossaro, A.; Mazzarello, R.; Rousseau, R.; Casalis, L.; Verdini, A.; Kohlmeyer, A.; Floreano, L.; Scandolo, S.; Morgante, A.; Klein, M. L.; Scoles, G. *Science* **2008**, *321*, 943−946.

(42) Barmparis, G. D.; Honkala, K.; Remediakis, I. N. *J. Chem. Phys.* **2013**, *138*, 064702.

(43) Fabris, L.; Antonello, S.; Armelao, L.; Donkers, R. L.; Polo, F.; Toniolo, C.; Maran, F. *J. Am. Chem. Soc.* **2006**, *128*, 326−336.

(44) Holm, A. H.; Ceccato, M.; Donkers, R. L.; Fabris, L.; Pace, G.; Maran, F. *Langmuir* **2006**, *22*, 10584−10589.

(45) Becucci, L.; Guryanov, I.; Maran, F.; Guidelli, R. *J. Am. Chem. Soc.* **2010**, *132*, 6194−6204.

(46) Perera, N. V.; Isley, W.; Maran, F.; Gascón, J. A. *J. Phys. Chem. C* **2010**, *114*, 16043−16050.

(47) Kaplan, J. M.; Shang, J.; Gobbo, P.; Antonello, S.; Armelao, L.; Chatare, V.; Ratner, D. M.; Andrade, R. B.; Maran, F. *Langmuir* **2013**, *29*, 8187−8192.

(48) Laredo, T.; Leitch, J.; Chen, M.; Burgess, I. J.; Dutcher, J. R.; Lipkowski, J. *Langmuir* **2007**, *23*, 6205−6211.

(49) Ramrez, P.; Andreu, R.; Cuesta, Á.; Calzado, C. J.; Calvente, J. J. *Anal. Chem.* **2007**, *79*, 6473−6479.

(50) Herne, T. M.; Tarlov, M. J. *J. Am. Chem. Soc.* **1997**, *119*, 8916−8920.

(51) Levicky, R.; Herne, T. M.; Tarlov, M. J.; Satija, S. K. *J. Am. Chem. Soc.* **1998**, *120*, 9787−9792.

(52) Lubin, A. A.; Plaxco, K. W. *Acc. Chem. Res.* **2010**, *43*, 496−505.

(53) Rant, U.; Arinaga, K.; Scherer, S.; Pringsheim, E.; Fujita, S.; Yokoyama, N.; Tornow, M.; Abstreiter, G. *Proc. Natl. Acad. Sci. U. S. A.* **2007**, *104*, 17364−17369.

(54) Xiao, Y.; Lai, R. Y.; Plaxco, K. W. *Nat. Protoc.* **2007**, *2*, 2875−2880.

(55) Drummond, T. G.; Hill, M. G.; Barton, J. K. *Nat. Biotechnol.* **2003**, *21*, 1192−1199.

(56) Hill, M. G.; Kelley, S. O. In *Bioinorganic Electrochemistry*; Hammerich, O., Ulstrup, J., Eds.; Springer: Dordrecht, The Netherlands, 2008; pp 129−160.

(57) Li, C.-Z.; Long, Y.-T.; Sutherland, T.; Lee, J. S.; Kraatz, H.-B. In *Frontiers in Biochip Technology*; Xing, W.-L., Cheng, J., Eds.; Springer: New York, 2006; pp 274−291.

(58) Caragheorgheopol, A.; Chechik, V. *Phys. Chem. Chem. Phys.* **2008**, *10*, 5029−5041.

DOI: 10.1021/ja5104475
J. Am. Chem. Soc. 2015, 137, 276−288

(59) Woehrle, G. H.; Brown, L. O.; Hutchison, J. E. *J. Am. Chem. Soc.* **2005**, *127*, 2172−2183.
(60) Song, Y.; Murray, R. W. *J. Am. Chem. Soc.* **2002**, *124*, 7096−7102.
(61) Warner, M. G.; Reed, S. M.; Hutchison, J. E. *Chem. Mater.* **2000**, *12*, 3316−3320.
(62) Gross, E.; Liu, J. H.; Alayoglu, S.; Marcus, M. A.; Fakra, S. C.; Toste, F. D.; Somorjai, G. A. *J. Am. Chem. Soc.* **2013**, *135*, 3881−3886.
(63) Gellman, A. J. *ACS Nano* **2010**, *4*, 5−10.
(64) Jenkins, S. J.; Pratt, S. J. *Surf. Sci. Rep.* **2007**, *62*, 373−429.
(65) Horvath, J. D.; Gellman, A. J. *Top. Catal* **2003**, *25*, 9−15.
(66) Pratt, S. J.; Jenkins, S. J.; King, D. A. *Surf. Sci.* **2005**, *585*, L159−L165.
(67) Attard, G. A. *J. Phys. Chem. B* **2001**, *105*, 3158−3167.

DOI: 10.1021/ja5104475
J. Am. Chem. Soc. 2015, 137, 276−288